Solid Earth Discuss., 5, 609–654, 2013
www.solid-earth-discuss.net/5/609/2013/
doi:10.5194/sed-5-609-2013

Solid Earth Discussions Open Access

Transport processes at quartz-water interfaces: constraints from hydrothermal grooving experiments

K. Klevakina[1], J. Renner[1], N. Doltsinis[2,3], and W. Adeagbo[2,4]

[1]Institut für Geologie, Mineralogie und Geophysik, Ruhr-Universität Bochum, 44780 Bochum, Germany
[2]Institut für Chemie, Ruhr-Universität Bochum, 44780 Bochum, Germany
[3]now at: Institut für Festkörpertheorie, Westfälische Wilhelms-Universität, 48149 Münster, Germany
[4]now at: Institut für Physik, Martin-Luther-Universität Halle-Wittenberg, 06120 Halle, Germany

Received: 25 March 2013 – Accepted: 16 April 2013 – Published: 22 April 2013

Correspondence to: J. Renner (joerg.renner@rub.de)

Published by Copernicus Publications on behalf of the European Geosciences Union.

Abstract

We performed hydrothermal annealing experiments on quartzite at temperatures of 392 to 568 °C and fluid pressures of 63 to 399 MPa for up to 120 h during which hydrothermal grooves developed on the free surfaces of the samples. Analysis of surface topology and groove characteristics with an atomic force microscope revealed a range of surface features associated with the simultaneous and successive operation of several processes partly depending on crystal orientation during the various stages of an experiment. Initially, dissolution at the quartzite-sample surface occurs to saturate the fluid in the capsule with SiO_2. Subsequently, grooving controlled by diffusion processes takes place parallel to dissolution and precipitation due to local differences in solubility. Finally, quench products develop on grain surfaces during the termination of experiments. Average groove-root angle amounts to about 80° and slightly depends on temperature, run duration, and misorientation between neighboring grains. The grooving is thermally activated, i.e., groove depth ranging from 5 nm to several micrometers for the entire suite of experiments generally increases with temperature and/or run time. We use Mullins' classical theories to constrain kinetics parameters for the transport processes controlling the grooving. In the light of previous measurements of various diffusion coefficients in the system SiO_2-H_2O, interface diffusion of Si is identified as the most plausible rate-controlling process. Grooving could potentially proceed faster if the fluid were not convecting in the capsule. Characteristic times of healing of microfractures in hydrous environments constrained from these kinetics parameters are consistent with the order of magnitude of time scales over which healing occurs in-situ according to geophysical surveys and of recurrence intervals of earthquakes.

1 Introduction

Quartz-filled veins of hydrothermal origin are common in rocks (e.g., Hilgers and Urai, 2002; Urai et al., 1991) documenting that SiO_2 is temporarily mobilized in the presence

SED
5, 609–654, 2013

of water. The quantitative description of dissolution, precipitation, and transport processes in the system SiO_2-H_2O is thus relevant for a general understanding of mass and energy transport in the Earth's crust and specifically of the creation and sealing of fluid conduits and requires experimental determination of various kinetics parameters (see for example Lasaga and Blum, 1986). Consequently, the thermodynamics of quartz-water mixtures have been the subject of research for at least half a century leading to constraints on solubility and dissolution kinetics of quartz in hydrous fluids (e.g., Gerya et al., 2005; Manning, 1994; Tester et al., 1994; Weill and Fyfe, 1964) as well as diffusion coefficients of silicon and oxygen in water and in quartz along different diffusion paths (e.g., Doltsinis et al., 2007a, b; Farver and Yund, 2000, 1991, 1995; Joesten and Fisher, 1988; Milke and Heinrich, 2002).

Grooves are a surface feature of polycrystalline aggregates that occurs in order to minimize surface energy. In material science, grooving studies have proven to be a valuable source for interface kinetics parameters (e.g., Mullins and Shewmon, 1959; Rabkin et al., 2006). The evolution of grooves is controlled by the transport and/or dissolution/precipitation kinetics of constituents. For the first time, the relation between the dominating diffusion process and groove geometry was formulated by Mullins (1957, 1960). Previous experimental studies on grooving characteristics were mostly performed on metals and alloys (Mullins and Shewmon, 1959; Rabkin et al., 2006, 2001) but some observations were reported for oxide ceramics (Saylor and Rohrer, 1999) and also minerals (Hay and Evans, 1983; Peters and Reimanis, 2003).

The objective of our exploratory study is to experimentally constrain the rate-controlling step and potentially the dominant transport mechanism for mobilization and deposition of SiO_2 at quartz-water interfaces at conditions relevant for the Earth's upper crust. For this end, we investigated hydrothermal grooving at the interface of quartz aggregates and water by analyzing geometrical groove characteristics as a function of time, temperature and pressure. In comparison to grooving studies in metals, this approach faced several complications due to sluggish equilibration between mineral and fluid, and orientation dependence of surface energy and/or diffusion coefficients

SED
5, 609–654, 2013

of a low symmetry mineral such as quartz. Therefore, we chose an approach employing polycrystalline aggregates with a large number of grain boundaries intersecting the surface in contact with fluid aiming at bulk statistical observations.

2 Background

2.1 Thermal grooving

When grain boundaries intersect an aggregate's surface, grooves tend to form due to minimization of interface energy. The geometry of the groove root is determined by the balance of the two surface tensions and the grain boundary tension and the constraint from the boundary tilt with respect to the free surface (Hackl et al., 2013; Herring and Conyers, 1951). In case the surface properties are independent of the orientation of the crystals, the following relation holds for the two angles at the root (Fig. 1)

$$\frac{\gamma_{gb}}{\gamma_s} = \cos\alpha_1 + \cos\alpha_2 \quad (1)$$

with γ_{gb} and γ_s denoting grain boundary energy and surface energy, respectively (Hackl et al., 2013). For grain boundaries intersecting the surface at a normal angle, we have $\alpha_1 = \alpha_2 \equiv \alpha$ and the root angle coincides with the dihedral angle α defined by

$$\cos\left(\frac{\alpha}{2}\right) = \frac{\gamma_{gb}}{2\gamma_s} \quad (2)$$

and commonly used as a quantification of the ratio between grain boundary energy and surface energy (e.g., Bailey and Watkins, 1950; Rabkin et al., 2001).

Equation (1) does not describe a stable equilibrium state but grooves will deepen with time while maintaining their geometrical characteristics. The actual surface evolution can be controlled by the kinetics of different atomistic transport processes. Mullins (1957, 1960) investigated grooving as controlled by the following diffusion paths:

SED
5, 609–654, 2013

(a) through the grain volume, (b) through the stagnant liquid in contact with the solid, and (c) along the solid-liquid interface. In addition, grooving by dissolution/evaporation was analyzed (Bokstein et al., 1995; Mullins, 1957). These early analyses were performed for monatomic materials with isotropic surface energy, dihedral angles independent of annealing time, and grain boundaries normal to the surface. The analytical solutions derived employing a small slope approximation yield self-similar evolution of groove geometry expressed by groove depth d and groove width w (Fig. 1) according to

$$d(t) = \lambda_d \cot\alpha (B_i t)^{1/n} \tag{3}$$

and

$$w(t) = \lambda_w (B_i t)^{1/n}. \tag{4}$$

The parameters B_i and λ_i depend on the dominant diffusion path (see Table 1). In particular, λ_w/λ_d amounts to 4.95 and 4.73 for $n = 3$ and 4, i.e., diffusion through the liquid and along the interface, respectively. Notably, the theory suggests that the occurrence and absence of humps on both sides of the grain boundary helps to discern between diffusion-controlled and dissolution-controlled grooves.

A number of analytical and numerical approaches extended Mullins' seminal work by considering large slopes (Robertson, 1971), anisotropy of surface energies (Zhang et al., 2004), tilted grain boundaries (Hackl et al., 2013; Min and Wong, 2006), diffusion in a multicomponent system (Dhalenne et al., 1979; Klinger, 2002), and the effect of mobile crystal defects (Rabkin et al., 2001). The geometry of the groove is sensitive to these extensions but general features of the Mullins' theory are mostly maintained while the absolute grooving kinetics is altered. When multi-component diffusion (Dhalenne et al., 1979; Klinger, 2002) takes place or time-dependence of interface energies is involved (Zhang et al., 2002), the growth exponent n may change considerably.

SED
5, 609–654, 2013

2.2 Solubility of SiO_2 in water and associated dissolution kinetics

The solubility of quartz in hydrous fluids is an important geochemical parameter and plays a major role both for planning our experiments and for their evaluation. At the start of an experiment, capsule charges consisting of a quartz sample and distilled water are in disequilibrium. With time, equilibrium is achieved by dissolution of the solid. Several questions have to be answered with respect to their consequences for groove evolution:

(a) How much SiO_2 goes into solution at what stage in a course of an experiment?

(b) After what time is equilibrium reached at p-T-conditions?

(c) Is the liquid likely to be stagnant in the capsule?

Below quantitative constraints on solubility and dissolution kinetics of quartz in water are therefore reviewed first and then the potential for convection in our capsules is analyzed.

2.2.1 Solubility of SiO_2 in water

The solubility of quartz in water and its dependence on temperature and pressure have been a subject of a number of experimental studies since the 1940ies (e.g., Fyfe and McKay, 1962; Gerya et al., 2005; Gratz and Bird, 1993; Morey et al., 1962; Weill and Fyfe, 1964). The solution of quartz in water was thought to proceed congruently and reversibly according to $SiO_{2(s)} + H_2O \Leftrightarrow H_4SiO_{4(aq)}$ (Manning, 1994). More recent work, however, indicates that polymerization of the silicic acid product may be significant for the dissolution process (Doltsinis et al., 2007a, b; Gerya et al., 2005). We rely on the quantitative description by Tester and Worley (1994) to describe the concentration at saturation, $m^{sat}_{H_4SiO_4}$ (mol_{SiO_2}/kg_{H_2O}) as a function of absolute temperature T and pressure p by

$$\log_{10} m^{sat}_{H_4SiO_4} = A + B \log_{10} V + C(\log_{10} V)^2 \quad (5)$$

SED
5, 609–654, 2013

with $A = -4.66206 + 0.0034063T + 2179.7T^{-1} - 1.1292 \cdot 10^{6}T^{-2} + 1.3543 \cdot 10^{8}T^{-3}$, $B = -0.00147180T - 806.97T^{-1}$, $C = 3.9465 \cdot 10^{-4}T$, and $V(p,T)$ ($\mathrm{cm^3\,g^{-1}}$) denoting the specific volume of water. The more recent quantitative relation by Gerya et al. (2005) yields modest deviations from Eq. (5) for our test conditions and we preferred Eq. (5) in order to use a consistent source for solubility and dissolution kinetics (see below). For our test conditions, we estimate concentrations of 0.0294 to 0.1025 $\mathrm{mol_{SiO_2}/kg_{H_2O}}$ that are reached by dissolving a layer of 0.3 to 6 µm from the entire surface or a single head face of a cylindrical sample with a diameter of 3 mm, respectively. In case dissolution were to occur preferentially at grain boundaries by groove etching at a single head face, these concentrations correspond to an average groove depth of several µm for a dihedral angle of about 80° and a polycrystalline aggregate with an average grain size of about 20 µm.

2.2.2 Dissolution kinetics of SiO_2 in water

On the basis of a large experimental data set, Tester (1994) derived the kinetics of quartz dissolution in water as

$$m(t) = m^{\mathrm{sat}}_{\mathrm{H_4SiO_4}} - (m^{\mathrm{sat}}_{\mathrm{H_4SiO_4}} - m^{0}_{\mathrm{H_4SiO_4}}) \exp\left(-\frac{kAt}{M m^{\mathrm{sat}}_{\mathrm{H_4SiO_4}}}\right) \quad (6)$$

with a rate constant

$$k = (276 \pm 193) \exp\left(-\frac{90.1 \pm 2.5\ \mathrm{kJ\,mol^{-1}}}{RT}\right) \frac{\mathrm{mol_{SiO_2}}}{\mathrm{m^2 s}}. \quad (7)$$

In Eq. (6), A ($\mathrm{m^2}$) denotes the active surface area, M (kg) the mass of water, t (s) time, and $m^{0}_{\mathrm{H_4SiO_4}}$ the initial concentration of silicic acid ($\mathrm{mol_{SiO_2}/kg_{H_2O}}$). We combined Eqs. (5)–(7) to evaluate the dissolution evolution in our experiments using the measured amounts of added water and the total surface area of a sample as active surface

SED
5, 609–654, 2013

area. Calculations accounting for the actual *p*-*T*-*t* evolution of the experiments indicate that equilibrium concentrations should be reached after 2.2 and 0.8 h at 392 and 568 °C, respectively.

3 Material and methods

3.1 Sample material, experimental apparatus and procedure

We used quartzite (novaculite from Arkansas, see Keller et al., 1977) with an average grain size of 20 to 30 µm in all experiments. Samples were prepared to cylindrical shape with a height of ∼ 4 mm and a diameter of ∼ 3 mm. One circular end face was sequentially polished to mirror quality first using SiC paper then diamond-oil paste down to 1 µm particle size. Two samples (see Table 2) were chemically polished with SITON for orientation analyses with the electron backscatter diffraction (EBSD) technique before the hydrothermal annealing experiments. The carbon coating applied for EBSD analysis was removed with a soft tissue before the actual annealing experiment. The effect of polishing procedure on grooving was addressed by preparing a sample with just one half of its surface experiencing the additional SITON-polishing.

Prepared quartzite cylinders were placed in gold capsules together with 16 to 35 µL distilled water. Capsules were welded shut under a binocular. Sealing was checked by heating capsules to 60 °C and monitoring their weight. Samples were annealed in a hydrothermal apparatus comprising an externally heated vessel. Vessel and capsules were oriented horizontal with their cylindrical axes. The heating rate was controlled to 20° min^{-1} and the cooling time from 580 to 40 °C temperature was about three hours reaching 300 °C after less than 24 min. Evaluating Eq. (6) for the actually employed heating rate indicates that the solution acquired 5 and 50 % of the saturation concentrations when reaching 392 and 568 °C, respectively.

Typically, samples experienced a single annealing run but some samples were repeatedly re-capsuled after intermittent investigations. We further varied the procedure

SED
5, 609–654, 2013

in several aspects to provide constraints on dissolution processes during our experiments. Some capsules were charged with silica gel or fine quartz powder in addition to the quartzite sample (see Table 2). These powders are expected to be preferentially dissolved compared to the quartzite.

The calculations regarding the time it takes for the fluid to equilibrate with the quartzite samples (see Sect. 2.2.2) were performed under the assumption that the bulk water does not flow in the capsule. However, when the water convects in the capsule, equilibration may proceed faster. Furthermore, continuous transport of solute from dissolution sites to precipitation sites may then occur for a fixed average concentration. Calibration runs constrained axial and radial gradients of 1.5 and 0.4 $^{\circ}$C mm^{-1}, respectively, yielding Rayleigh numbers (Siggia, 1994) of $> 10^6$ for our assembly strongly suggesting the occurrence of convection.

3.2 Determination of groove characteristics

After the hydrothermal annealing, the previously polished end faces of samples were studied by light and atomic force microscopy (AFM, XE-100 PSIA). The AFM measurements were performed in contact mode using cantilevers with nominal tip radius of 10 nm (910M-NSC36, 910M-SICONA). Generally, square areas of 90 µm edge length were scanned with a frequency between 0.4 and 0.6 Hz and a grid spacing of $\sim$ 0.18 µm. The horizontal step size causes an uncertainty in groove depth of less than 25 nm for the encountered dihedral angles. With the use of smaller scan areas a higher lateral resolution can be achieved and thus a better groove depth resolution. However, the chosen area constitutes a reasonable compromise between scan duration and accuracy given that individual grooves vary considerably in their properties anyway.

In the vast majority of cases, geometrical groove characteristics were derived from averaged profiles. Averaging was gained from overlaying the groove trace with a rectangle with its long edges parallel to the trace and stacking all perpendicular transects within the rectangle. The variability of the groove characteristics within a chosen rectangle can be substantial, i.e. ±50 % in depth. This large variability results mostly from

SED
5, 609–654, 2013

blunt roots possibly due to precipitated quench materials. In less than 10 %, we had to rely on single scan profiles for the determination of depth, width, and groove-root angle because averaging failed due to poor surface quality. The quoted average groove characteristics are considered reliable representations of the depth and the groove-root angle to within about ±15 % and ±5°, respectively. The effects of scan direction (relative to groove) and frequency do not further increase the uncertainty in groove characteristics. Results represent averages and standard deviations for the averaged parameters gained from investigating 100 up to 600 grooves for a single sample.

3.3 Grain orientation analysis

The orientation of individual grains relative to the sample surface and to their neighbors (misorientation) were determined by the electron backscatter diffraction (EBSD) technique using a LEO 1530 scanning electron microscope (SEM) with field emission gun. The SEM was operated at an accelerating voltage of 20 kV with a working distance of 25 mm to the sample surface tilted at an angle of 70°. Indexing and processing was performed by the CHANNEL5 HKL software. The misorientation between individual grains was determined with Stereo32. Here we restrict ourselves to characterizing only pairs of grains for which a single angle expresses the associated misorientation. The relation between neighboring grains that both exhibit *c*-axes normal to their surfaces (within ±10°) is expressed by the angle enclosed by the two *a*-axes. Grains with either the *a*-axis or the *b*-axis normal to their surface (within ±10°) are characterized by the angle enclosed by their *c*-axes.

4 Experimental results

A total of 25 "standard" annealing experiments were performed at temperatures of 392, 441, 490, and 568 °C and pressures from 63 to 399 MPa for durations up to 120 h (Table 2). In addition, we ran two sequential anneals, three experiments with added

SED
5, 609–654, 2013

powders, and one with altered sample geometry. In the following, we first present the general morphological observations of hydrothermally annealed surfaces as found by optical and atomic force microscopy. Then, the quantified average groove characteristics are reported considering also the effect of variations in experimental procedure.

4.1 Phenomenological observations

Groove development and growth with increasing annealing duration (and temperature or pressure) are already visible with the light microscope (Fig. 2). Yet, the initially flat and mirror-quality polished surfaces exhibit in addition scratches, significant topography due to grains at different heights, pocks, holes, and roughness of individual grains after annealing (Fig. 3). In cases, individual grain surfaces are not parallel to the general sample surface but tilted. The frequency with which these features occur varies with annealing conditions. Qualitatively, we do not find a significant difference in surface characteristics of samples that experienced a single anneal and samples that were repeatedly annealed with intermittent quenching for AFM analysis. For the latter, individual grooves could be tracked over a sequence of as much as three annealing steps. The number of tractable grooves is limited by plug-out of grains and increasing surface roughness.

Scratch traces are prominent after the shortest annealing times indicating that the polishing procedure fills surface irregularities with highly soluble material (Fig. 3a). Scratches tend to occur on high lying grains after short annealing times while scratches occur preferentially on low lying grains after extended annealing. The depth of individual scratches and consequently the number of scratch traces decrease with increasing annealing. Likely, this healing, driven by surface energy reduction, proceeds by local transport processes.

With extended annealing, pocks and pits are typically present on low and high lying grains, respectively. The large number of closely spaced pocks (Fig. 3d) and holes partly resembling dislocation etch pits (Fig. 3b) lets individual grains appear roughened at their surface (Fig. 3f). Groove and step evolution are affected by polishing treatment

SED
5, 609–654, 2013

and addition of quartz powder or gel. Experiments on SITON-polished samples with added powders tend to yield surfaces with more pronounced roughness than experiments on SITON-polished samples without added powder.

Several structures depend on the orientation of individual grains: dislocation etch pits, deformation lamellae, faceting, and terraced growth. The SEM images of some samples annealed at 568 °C and 260 MPa for 47 h document the growth of surfaces with specific orientations yielding the typical habitus of hydrothermally grown quartz crystals (Fig. 5). To specify the relation between surface orientation and surface structure, two samples were scanned with EBSD before annealing (see Table 2). We focused on three low-index surfaces $\{0001\} \equiv c$, $\{10\bar{1}0\} \equiv b$, and $\{11\bar{2}0\} \equiv a$ and defined different grain boundary types between neighboring grains with one of these axes perpendicular to the surface within ±10° (i.e., "*a*/*c* boundary" is a boundary between two grains, one with the *a*-axes and one with the *c*-axes approximately perpendicular to the surface). The two samples differ in surface structure and height variations of grains. For the experiment run at 392 °C (P57, Table 2), the {0001} surfaces show pronounced roughness and constitute the relatively high lying surfaces, while the prism surfaces $\{10\bar{1}0\}$ appear relatively low, yet smooth with some scratches (Fig. 4a–c). The asymmetry of grooves is larger for *a*/*c* boundaries than for *a*/*b* boundaries. The relative height of {0001} and $\{10\bar{1}0\}$ surfaces is inversed for the experiment run at the higher temperature of 568 °C (P42, Fig. 4d–f). At this temperature, the majority of grain surfaces are flat and scratches are absent.

4.2 Groove characteristics

Observed groove-root angles widely range from 40 to 90° but angles of about 80° dominate. The bulk data set indicates a tendency for slightly decreasing angles with increasing annealing time (angles of 81 to 88 and 74 to 83 are most frequent for experiments run at 392 °C and at 568 °C, respectively), an observation that seems to be confirmed by the sequential annealing experiments (Fig. 6). This decrease becomes

SED
5, 609–654, 2013

more apparent the higher the annealing temperature. We find some evidence for a systematic relation between root angle and crystallographic orientation of neighboring grains; angles are lowest for intermediate misorientation (Fig. 7).

Grooves exhibit a range of geometries even in a single experiment (Fig. 8). We find grooves with and without steps (i.e., differences in height between neighboring grains) as well with and without the humps typical for diffusion-controlled groove evolution. We did not develop strict criteria but visual inspection and exemplary statistics suggest the following typical inventory. The shape of about 15 % of the grooves is so biased by surface roughness of the enclosing grains that a characterization is impossible. Of the remaining grooves, 10 to 20 % exhibit clearly visible humps and < 10 % would be characterized as dissolution grooves (Fig. 9). About half of all grooves are of mixed/intermediate character, i.e., steps and tilting make characterization difficult. This inventory is rather insensitive to annealing conditions.

While groove depth scatters considerably for a single experiment, its average systematically increases with increasing temperature, annealing time, and pressure. The frequency distributions of groove depths typically exhibit a maximum at the smallest depth bin and a continuous decrease towards deeper grooves. A detailed statistical analysis for experiments run at 392 °C reveals that the groove depth for dissolution grooves, i.e., without humps, are modestly less deep than grooves with distinct humps. The growth-enhancing effect of pressure is reflected by average groove depths that approximately double for a doubling in pressure. Adding SiO_2-powder to a capsule leads to deeper grooves and larger steps compared to experiments with only water in the capsules (compare P36 and P44 in Table 2).

Independent of annealing conditions, many grooves deviate from the relations between depth and width according to Mullins (1960). Groove width is generally too low for the observed depth and a fairly systematic frequency distribution is found for the difference between observed groove geometries and predictions of the Mullins' theory (Fig. 10). The deviation of the ratio between width and depth of individual grooves from

SED
5, 609–654, 2013

the theoretical ratio between 4.73 and 4.95 (see Eqs. 5, 6) exhibits a maximum from 1 to 2.5.

The statistics of the ratio between step height and groove depth (h/d) evolves with annealing time (Fig. 11). Samples from short experiments are dominated by a large step-depth ratio. With increasing annealing time, the number of steps decreases and grooves become relatively deeper compared to steps. Finally, we observe many steps with deep grooves (small h/d) for samples of the longest experiments.

In sequential annealing experiments, grooves deepen systematically (Fig. 6). Similarly, the height of the many steps systematically increases with the number of sequences reaching up to 400 nm, a magnitude not observed for single anneals even after the longest durations. The growth rate of grooves is significantly larger for sequential anneals than for a suite of single anneals (Fig. 13).

5 Discussion

Our experiments are complicated due to the non-equilibrium starting conditions and the likely occurring convection in the capsules. Therefore, it is mandatory to develop a plausible scenario of process sequences from the observations before actually attempting to constrain kinetics of individual processes.

5.1 Process sequence in experiments

We tentatively distinguish three phases. First, dissolution processes are active predominantly during heating but also slightly beyond until the liquid is saturated in SiO_2. Second, dissolution-precipitation processes and grooving occur simultaneously at constant bulk composition of the liquid. The grooving involves diffusion processes to some extent as evidenced by the humps flanking a fraction of the grooves. Finally, precipitation may occur during the reduction in temperature and pressure when terminating an experiment.

SED
5, 609–654, 2013

The initial dissolution processes active until saturation of the liquid is reached are heterogeneous as documented by the steps exhibiting orientation-dependent heights. At this stage, grains with the *c*-axes perpendicular to their surface seem to be most prone to dissolution. The survival of scratch traces on the high laying surfaces (inferred to be $\{10\bar{1}0\}$, Fig. 3a) indicates subordinate dissolution of these surfaces in short experiments.

The optical observations with respect to scratch occurrence and intensity are consistent with the dependence of step development on temperature and annealing time. The increase in step height with every new heating stage of sequential annealing experiments supports our notion of preferred solution of specific surfaces. The initial topographic characteristics are affected by polishing treatment and the addition of quartz powder. While grooves remain very shallow during the saturation stage, grooves are deeper when SiO_2 powder is added to the charge than when it is not. Apparently, a finite amount of the entire surface is dissolved from samples when no powder is added. This bulk dissolution masks the grooving, i.e., the grooves do not significantly "outrun" the dissolution front. Yet, when powder is added saturation is likely achieved by dissolving preferentially the powder and grooving is more prominent right from the start. The differences in early groove depth between the two charge types is consistent with our estimates (see 2.2.1) on how thick a layer of a sample surface had to be removed to reach saturation from an order of magnitude perspective.

The second stage is characterized by increasing groove depth, an inversion of individual steps but also by the occurrence of pocks on some surfaces. Furthermore, the number of steps and dissolution grooves tend to decrease at the beginning of this phase (Fig. 9). In contrast to the initial stage during which massive disequilibrium between the liquid and the solid triggers all possible dissolution processes, now also precipitation takes place as likely evidenced by the pocks and balances ongoing dissolution driven by subtle differences in solubility between surfaces of different orientations and between intact lattice and defects. Previously preferentially dissolved grains with the *c*-axes normal to their surface now apparently grow as indicated by the pocks with

SED
5, 609–654, 2013

prismatic habitus (Figs. 3c and 5 right) leading to increasing roughness when becoming ubiquitous. This switch may be related to a contrasting order of dissolution kinetics and surface energy for the low index orientations. The precise nature of the temperature and time dependence of these dissolution processes is unclear. Furthermore, the necessary local transport of the solid's constituents between "neighboring" grains may be affected by convection in the capsule.

Finally, the cooling phase should be characterized by precipitation processes since the fluid is oversaturated. We tentatively link at least some of the isolated pocks with this stage (Fig. 3d) because qualitatively some variation in their occurrence seems to be related to only a part of the sample surface being in contact with oversaturated liquid during cooling when critical conditions are passed.

5.2 Groove geometry and constraints on kinetics parameters

Root angles of groove constitute a prominent quantitative measure of groove geometry constraining the ratio of involved interface energies albeit approximately. Orientation dependence of surface energy is indicated by the observed relations between grain level and orientation and between groove-root angle and misorientation of neighboring grains (Fig. 7) showing some similarity to observations made for ice (Suzuki and Kuroiwa, 1972). On average, measured groove-root angles tend to be a few degrees larger than previously reported dihedral angles (Holness, 1992; Holness, 1993). Also, we noted a tendency for slightly decreasing root angles with increasing annealing time (Fig. 6). Both observations are opposite to expectations due to the difference between the true dihedral angle as an energy ratio and the groove-root angle of tilted boundaries (Hackl et al., 2013) when speculating that grain boundaries tend to intersect the surface at a normal angle with increasing annealing time as known from thin films (e.g. Thompson, 1990). The larger boundary tilt the more groove-root angles fall short of dihedral angles (Hackl et al., 2013). Thus, one would rather expect to see an increase in groove-root angle with time. Alternatively, evolution in grain boundary-surface energy

SED
5, 609–654, 2013

ratio due to impurity segregation, for example, has been invoked as an explanation for the change in groove-root angle with time (Zhang et al., 2002).

In the quest for kinetics parameters for the surface evolution, one can either analyze the entire profile of individual grooves or rely on the variation of statistical groove characteristics with experimental conditions. The various approximate approaches of Mullins (1957, 1960) have the advantage of providing analytical expressions for groove profiles. We fit these analytical expressions to selected observed profiles to constrain kinetics parameters (see examples in Fig. 12). Note, asymmetry is not predicted by any of the Mullins theories. For such grooves and also grooves with steps, extended approaches have to be considered (e.g., Rabkin et al., 2001) that however lack analytic expressions suitable for our fitting exercise. Therefore, we simplistically treat the two groove flanks independently and prescribe the dihedral angle of the analytical expression by the actually observed angle between groove flank and the normal to the flat surface.

A large number of grooves are best fit by the dissolution geometry. Individual grooves however exhibit better resemblance to one of the two others of the three potential analytical profiles (dissolution, surface diffusion, diffusion through liquid). From these, kinetics parameters were determined for the two alternative processes, surface diffusion and diffusion through the liquid (Fig. 13). The resulting diffusion coefficients range from 10^{-11} to $10^{-13}\,m^2\,s^{-1}$.

In order to complement and further substantiate these results, we selected a subset of the standard "single-anneal" experiments for which polishing was identical to fit evolution laws to averaged groove depth and (half-)width. The two groove sides are again treated separately and among the many grooves we used only those whose depth-width ratio agrees with the average of 4.84 of the theoretical Mullins values (4.73 and 4.95, see Eqs. 2 and 3) within ±0.1. As noted above, groove widths are generally too low in comparison to observed depths, i.e., many grooves exhibit depth-width ratios < 4.73 (Fig. 10). Grain boundary sliding due to assimilation of dislocations tends to reduce the width of grooves compared to the Mullins theory (Rabkin et al 2001), yet

SED
5, 609–654, 2013

this mechanism likely plays no role in our experiments given the low homologous temperatures. Despite the variability of groove characteristics in a single experiment this subset of observations represents thermally activated groove growth (Fig. 10). At face value, the measured data follow relatively large growth exponents in comparison to the theoretically values of 3 or 4 (Fig. 13). Sequential annealing experiments were not considered for this exercise since the change of groove geometry with time differs significantly from single anneals (Fig. 13) likely due to the repeated dissolution at sample surfaces when a sample is repeatedly heated in the presence of distilled water.

Kinetics parameters quoted in Table 3 (pre-factor D_0, apparent activation enthalpy, apparent activation volume) were deduced by non-linear inversion (Sotin and Poirier, 1984) employing Eqs. (3) and (4) for the three alternative diffusion paths (through the liquid, along the solid-liquid interface, through the solid) and fixing the growth exponent *n*accordingly. The quoted ranges in the kinetics parameters reflect the experimental uncertainties (see Fig. 13 for a relation between model curves and observations). For the inversion every experiment is characterized by a set of values for groove depth, groove width, groove-root angle, temperature, time, and pressure and we use the found standard deviation as a measure of uncertainty for the geometrical groove parameters while pressure, temperature and time are assigned accuracies of 20 MPa, 10 °C, and 5 min, respectively. Molecular volume, grain boundary width, surface energy, thickness of the layer in which surface diffusion takes place, and equilibrium concentration of solute in the solvent are assumed known parameters for the inversion (see Table 1). Order of magnitude-wise, the inverted diffusion coefficients are similar to the ones derived from the analysis of individual groove profiles but are several orders of magnitude too large in comparison to literature values for Si-diffusion in quartz yet too small in comparison to estimates for the diffusion coefficient of Si through H_2O (Fig. 14). Our calculations for the case of diffusion preferentially along solid-liquid interfaces are fairly close to previously reported results for Si diffusion along wet grain boundaries or interface diffusion.

The activation energies found from the various models range from 88 to 159 kJ mol^{-1} (Table 3). Specifically, for interface diffusion we estimate an activation energy of

SED
5, 609–654, 2013

$132 \pm 25\,kJ\,mol^{-1}$ in close agreement with the activation energy of $137 \pm 18\,kJ\,mol^{-1}$ for diffusion of Si – the slower of the two components Si and H (Farver and Yund, 1991) – along wet grain boundaries (Farver and Yund, 2000). The activation energy here deduced for grooving dominated by diffusion through the liquid ($115 \pm 23\,kJ\,mol^{-1}$) largely exceeds the currently available constraints on the activation energy for Si diffusion through water for which Watson and Wark (1997) estimate about $21\,kJ\,mol^{-1}$ from an evaluation of the Stoke-Einstein relation between diffusion coefficient and viscosity while their experimental data yield $52 \pm 9\,kJ\,mol^{-1}$ at temperatures of 530 °C to 800 °C and a pressure of 1 GPa. A single observation at 0.6 GPa indicates a subordinate effect of pressure.

The range of activation energies found here further mostly exceeds previously reported values for the activation energy of dissolution, $89 \pm 5\,kJ\,mol^{-1}$ (Tester et al., 1994), $71 \pm 9\,kJ\,mol^{-1}$ (Dove and Crerar, 1990), and 67 to $77\,kJ\,mol^{-1}$ (Rimstidt and Barnes, 1980). These rather low values likely document that dissolution of real crystals is dominated by processes at crystal defects (see discussion by Adeagbo et al., 2008; Dove and Crerar, 1990). By ab initio molecular dynamics simulations, Adeagbo et al. (2008) found a barrier for the dissolution of SiO_2 from a perfect, defect free crystal surface of about $186\,kJ\,mol^{-1}$ representing breakage of the first Si-O bond in fair agreement with the prediction of $228\,kJ\,mol^{-1}$ for breaking Si-O bonds gained by dividing the heat of formation of SiO_2 by the coordination of Si. Probably constituting the opposite extreme to a perfect crystal, modeling of the hydroxylation of $Si(OH)_4$ in the gas phase by Lasaga and Gibbs (1990) yield a lower activation energy ranging between 64 and $120\,kJ\,mol^{-1}$ more closely agreeing with the experimentally derived values.

The apparent activation volumes gained for the various models all range at about $-100\,cm^3\,mol^{-1}$ (Table 3), i.e., about four times the molecular volume of quartz. At face value, such large activation volumes are not easily related with any of the discussed processes.

The compilation of available diffusion coefficients in the system SiO_2-H_2O (Fig. 14) strongly suggests that Si-transport through the fluid should be the fastest path for the

SED
5, 609–654, 2013

slowest constituent and thus rate-limiting if grooving were controlled by diffusion. However, the current constraints on the kinetics of Si-diffusion through H_2O (Adeagbo et al., 2008; Doltsinis et al., 2007a) suggest much faster groove growth for the conditions of our experiments than we actually observed. Furthermore, the observed strong effect of pressure on grooving is at odds with Watson and Wark's (1997) inference that Si-diffusion through water is insensitive to pressure further supporting the interpretation that diffusion through the liquid is not the rate-controlling process in our experiments.

In principle, any step in the chain dissolution – transport – precipitation could be rate limiting. Per-se, a control by interface reaction kinetics either of the dissolution or the precipitation step cannot be excluded. In our experiments, Si-concentration gradients in the liquid above the solid-liquid interface are likely continuously disturbed by convection. Continuous advection of dissolved atoms may therefore cause some deepening of grooves to be controlled by dissolution driven by local differences in solubility. The numerical coincidence of the apparent activation energies derived from dissolution-precipitation creep experiments on quartz aggregates under hydrous conditions and that of dissolution kinetics was considered evidence for dissolution as controlling the rates of this "deformation by mass transfer" (Dewers and Hajash, 1995; Gratier and Guiget, 1986; Niemeijer et al., 2002; Schutjens, 1991). The discussions presented in the deformation studies excluded diffusion through the liquid, the only considered alternative, due to the large deviation between activation energies of dissolution kinetics (about 80 $kJ\,mol^{-1}$) and diffusion in the liquid (10 to 20 $kJ\,mol^{-1}$). Yet, alternatively a diffusion process that does not require a dissolution step maybe rate-controlling, i.e., interface diffusion or lattice diffusion. Of these two diffusion paths, interface diffusion appears much more likely given the constraints on lattice diffusion kinetics and in fact our estimates for interface diffusion coefficients are fairly compatible with previously reported values (Fig. 14). In conclusion, groove geometry (presence/absence of humps) as well as characteristics of groove development (activation energy) indicate that a diffusion process is involved that leads to grooving rates at least comparable to the surface alterations associated with coeval dissolution processes.

SED
5, 609–654, 2013

5.3 Implications

The gained constraints on transport kinetics in the system SiO_2-H_2O at conditions representing a depth of 10 to 20 km in the continental crust can be used to discuss the characteristics of microstructural alterations, such as crack healing in hydrothermal environments, and associated recovery (e.g., Tenthorey et al., 2003). From a micromechanical perspective, healing and sealing of cracks involves a sequence of modifications first of planar then of cylindrical void surfaces and it has been suggested that the ovulation of cylindrical pores due to the Rayleigh–Taylor instability (Nichols, 1976) is rate-controlling in this complex process (e.g., Smith and Evans, 1984). The ovulation in turn is controlled by the same kinetics parameters as hydrothermal grooving. Therefore, we use the derived constraints on kinetics parameters to estimate the characteristic time of ovulation. This estimate constitutes an upper bound for the "real" time since – as explained above – the derived kinetics parameters represent situations involving non-stagnant fluids. When fluids were at rest in the cracks, healing could potentially proceed much faster by diffusion of Si through the liquid. The activation energy for crack healing of $80 \pm 26\,\mathrm{kJ\,mol^{-1}}$ experimentally determined at conditions comparable to ours (Brantley et al., 1990) overlaps with our estimated activation energy for interface diffusion (Table 3) but also with the range reported for dissolution kinetics.

For a cylinder of radius R, the characteristic time τ for the first ovulation is given by

$$\tau \simeq 6.6 \frac{R^4}{B_s} \tag{8}$$

when the cylinder geometry exceeds a critical aspect ratio and surface alteration is kinetically controlled by surface (interface) diffusion with the kinetics parameter B_s defined in Table 1. Relying on Eq. (8) and our constraints on kinetics parameters (Table 3), predicted characteristic times range from weeks to centuries depending on temperature and pressure (Fig. 15). One class of models for occurrence and recurrence of mid-crustal earthquakes (e.g., Gratier et al., 2002) rests on "cyclic" variations in effective stresses due to dilation and permeability increase associated with crack generation

SED
5, 609–654, 2013

and subsequent healing and permeability reduction (e.g., Brantley et al., 1990; Morrow et al., 2001). In this context, our estimate for healing times should be comparable to the order of magnitude of recurrence intervals and the times over which substantial healing occurs as deduced from geophysical surveys (e.g., Li et al., 1998, 2006; Peng and Ben-Zion, 2006). The range of characteristic healing times deduced from this study (Fig. 15) seems fairly comparable to if not somewhat larger than the field observations. An overestimation is notably consistent with the expectation that the transport kinetics for non-stagnant fluids derived here yield upper bounds for characteristic times of healing. The order of magnitude consistency between our predictions and observations should be taken as motivation for more detailed studies since clearly a number of factors -not accounted for here- may affect healing, such as differences between fluid pressure and total pressure or directed loading and chemical composition.

6 Conclusions

We experimentally explored the potential of investigating surface grooving of quartzite samples in a hydrothermal environment for providing constraints on transport paths and associated kinetics parameters of processes controlling the evolution of the solid's surface. In principle analyses of grooves bears a great potential for constraining needed kinetics parameters, yet, several complications are encountered in this approach. Disequilibrium in capsule requires dissolution until saturation causing surface alterations masking the early stages of grooving. Dissolution-precipitation processes due to local differences in solubility prevail after saturation of the fluid and convection takes place continuously at experimentally realizable thermal gradients. It is not clear whether convection simply hinders the development of concentration gradients in the fluid that reflect the surface curvature or whether – and if so to what extent – convection contributes to ongoing dissolution-precipitation processes. Finally, quartz with its low symmetry exhibits considerable orientation dependence in surface energy, dissolution-precipitation kinetics, and likely also in surface diffusion coefficients.

SED
5, 609–654, 2013

Potentially, sequential experiments on bi-crystals with specific orientations may help to reach firmer specific conclusions than in our approach employing polycrystalline aggregates. Nevertheless, bulk kinetics parameters were constrained that likely quantify surface diffusion of Si at hydrothermal conditions. Results of micromechanical modeling of microcrack healing using the derived kinetics parameters compare reasonably well with evidence for healing from geophysical surveys and recurrence intervals of mid-crustal earthquakes.

Acknowledgements. We gratefully acknowledge funding by the German science foundation. W. Maresch and S. Chakraborty generously permitted usage of the hydrothermal vessel operated by the petrology group at RUB. Sincere thanks go to J. ter Heege for unselfishly sharing characterization information on the used novaculite, R. Neuser for his support during SEM work, F. Bettenstedt for excellently preparing the samples and maintaining the test equipment.

References

Adeagbo, W. A., Doltsinis, N. L., Klevakina, K., and Renner, J.: Transport processes at α-quartz-water interfaces: Insights from first-principles molecular dynamics simulations, Chem. Phys. Chem., 9, 994–1002, 2008.

Bailey, G. L. J. and Watkins, H. C.: Surface tensions in the system solid copper-molten lead, P. Phys. Soc. B, 63, 350, doi:10.1088/0370-1301/63/5/306, 1950.

Bokstein, B. S., Klinger, L. M., and Apikhtina, I. V.: Liquid grooving at grain boundaries, Mater. Sci. Eng. A-Struct., 203, 373–376, 1995.

Brantley, S. L., Evans, B., Hickman, S. H., and Crerar, D. A.: Healing of microcracks in quartz – implications for fluid flow, Geology, 18, 136–139, 1990.

Dewers, T. and Hajash, A.: Rate equations for water-assisted compaction and stress induced water-rock interaction in sandstones, J. Geophys. Res., 100, 13093–13112, 1995.

Dhalenne, G., Revcolevschi, A., and Monty, C.: Grain boundaries in NiO. II. Determination of mass transport mechanisms by thermal grooving, Phys. Status Solidi A, 56, 623–636, 1979.

Doltsinis, N. L., Burchard, M., Maresch, W. V., Boese, A. D., and Fockenberg, T.: Ab initio molecular dynamics study of dissolved SiO_2 in supercritical water, J. Theor. Comput. Chem., 6, 49–62, 2007a.

Doltsinis, N. L., Maresch, W. V., Burchard, M., and Fockenberg, F.: Dissolved quartz in supercritical water: Insights from ab initio molecular dynamics simulations, Goldschmidt 2007 Cologne, A230–A230, 2007b.
Dove, P. M. and Crerar, D. A.: Kinetics of quartz dissolution in electrolyte solutions using a hydrothermal mixed flow reactor, Geochim. Cosmochim. Ac., 54, 955–969, doi:10.1016/0016-7037(90)90431-J, 1990.
Farver, J. and Yund, R.: Silicon diffusion in a natural quartz aggregate: constraints on solution-transfer diffusion creep, Tectonophysics, 325, 193–205, 2000.
Farver, J. R. and Yund, R. A.: Oxygen diffusion in quartz – dependence on temperature and water fugacity, Chem. Geol., 90, 55–70, 1991.
Farver, J. R. and Yund, R. A.: Grain-boundary diffusion of oxygen, potassium and calcium in natural and hot-pressed feldspar aggregates, Contrib. Mineral. Petr., 118, 340–355, 1995.
Fyfe, W. S. and McKay, D. S.: Hydroxyl ion catalysis of crystallization of amorphous silica at 330 degrees C and some observations on hydrolysis of albite solutions, Am. Mineral., 47, 83–89, 1962.
Gerya, T. V., Maresch, W. V., Burchard, M., Zakhartchouk, V., Doltsinis, N. L., and Fockenberg, T.: Thermodynamic modeling of solubility and speciation of silica in H_2O-SiO_2 fluid up to 1300 degrees C and 20 kbar based on the chain reaction formalism, Eur. J. Mineral., 17, 269–283, 2005.
Gratier, J. P. and Guiget, R.: Experimental pressure solutiondeposition on quartz grains: the crucial effect of the nature of the fluid, J. Struct. Geol., 8, 845–856, 1986.
Gratier, J.-P., Favreau, P., Renard, F., and Pili, E.: Fluid pressure evolution during the earthquake cycle controlled by fluid flow and pressure solution crack sealing, Earth Planets Space, 54, 1139–1146, 2002.
Gratz, A. J. and Bird, P.: Quartz dissolution: Theory of rough and smooth surfaces, Geochim. Cosmochim. Acta, 57, 977–989, 1993.
Hackl, K., Fischer, F. D., Klevakina, K., Renner, J., and Svoboda, J.: A variational approach to grooving and wetting, Acta Mater., 61, 1581–1591, 2013.
Hay, R. S. and Evans, J. B.: Grain boundary grooving of calcite bicrystals Proceedings of the 24th US symposium on rock mechanics; theory, experiment, practice 24, 469–472, 1983.
Herring, C. and Conyers: Some theorems on the free energies of crystal surfaces, Phys. Rev., 82, 87–93, 1951.

SED
5, 609–654, 2013

Hilgers, C. and Urai, J. L.: Microstructural observations on natural syntectonic fibrous veins: implications for the growth process, Tectonophysics, 352, 257–274, 2002.
Holness, M. B.: Equilibrium dihedral angles in the system quartz-CO_2-H_2O-NaCl at 800 °C and 1–15 kbar: the effects of pressure and fluid composition on the permeability of quartzites, Earth Planet. Sci. Lett., 114, 171–184, 1992.
Holness, M. B.: Temperature and pressure dependence of quartz-aqueous fluid dihedral angles: the control of adsorbed H_2O on the permeability of quartzites, Earth Planet. Sci. Lett., 117, 363–377, doi:10.1016/0012-821X(93)90090-V, 1993.
Joesten, R. and Fisher, G. W.: Kinetics of diffusion controlled mineral growth in the Christmas Mountains (Texas) contact aureole, Geol. Soc. Am. Bull., 100, 714–732, 1988.
Keller, W. D., Viele, G. W., and Johnson, C. H.: Texture of Arkansas Novaculite indicates thermally induced metamorphism, J. Sediment. Res., 47, 834–843, doi:10.1306/212F7266-2B24-11D7-8648000102C1865D, 1977.
Klinger, L.: Grain boundary grooving in two component system, Acta Mater., 50, 3358–3395, 2002.
Lasaga, A. C. and Blum, A. E.: Surface chemistry, etch pits and mineral-water reactions, Geochim. Cosmochim. Ac., 50, 2363–2379, doi:10.1016/0016-7037(86)90088-8, 1986.
Lasaga, A. C. and Gibbs, G. V.: Ab-initio quantum mechanical calculations of water-rock interactions: Adsorption and hydrolysis reactions, Am. J. Sci., 290, 263–295, 1990.
Li, Y.-G., Vidale, J. E., Aki, K., Xu, F., and Burdette, T.: Evidence of Shallow Fault Zone Strengthening After the 1992 M7.5 Landers, California, Earthquake, Science, 279, 217–219, doi:10.1126/science.279.5348.217, 1998.
Li, Y. G., Chen, P., Cochran, E. S., Vidale, J. E., and Burdette, T.: Seismic evidence for rock damage and healing on the San Andreas Fault associated with the 2004 M 6.0 Parkfield Earthquake, Bull. Seism. Soc. Am., 96, S349–S363, doi:10.1785/0120050803, 2006.
Manning, C. E.: The solubility of quartz in H_2O in the lower crust and upper-mantle, Geochim. Cosmochim. Ac., 58, 4831–4839, 1994.
Milke, R. and Heinrich, W.: Diffusion-controlled growth of wollastonite rims between quartz and calcite: comparison between nature and experiment, J. Metamorph. Geol., 20, 467–480, 2002.
Min, D. and Wong, H.: Grain-boundary grooving by surface diffusion with asymmetric and strongly anisotropic surface energies, J. Appl. Phys., 99, 023515, doi:10.1063/1.2159082, 2006.

SED
5, 609–654, 2013

Morey, G. W., Fournier, R. O., and Rowe, J. J.: The solubility of quartz in water in the temperature interval from 25-degrees to 300-degrees-C, Geochim. Cosmochim. Ac., 26, 1029–1043, 1962.
Morrow, C. A., Moore, D. E., and Lockner, D. A.: Permeability reduction in granite under hydrothermal conditions, J. Geophys. Res., 106, 30551–30560, 2001.
Mullins, W. W.: Theory of thermal grooving, Appl. Phys., 28, 333–339, 1957.
Mullins, W. W.: Grain boundary grooving by volume diffusion, Trans. Metall. Soc., 218, 354–631, 1960.
Mullins, W. W. and Shewmon, P. G.: The kinetics of grain boundary grooving in copper, Acta Metall. Mater., 7, 163–170, 1959.
Nichols, F. A.: On the spheroidization of rod-shaped particles of finite length, J. Mater. Sci., 11, 1077–1082, 1976.
Niemeijer, A. R., Spiers, C. J., and Bos, B.: Compaction creep of quartz sand at 400–600 °C: experimental evidence for dissolution-controlled pressure solution, Earth Planet. Sci. Lett., 195, 261–275, 2002.
Peng, Z. and Ben-Zion, Y.: Temporal changes of shallow seismic velocity around the Karadere-Duzce branch of the north Anatolian fault and strong ground motion, Pure App. Geophys., 163, 567–600, doi:10.1007/s00024-005-0034-6, 2006.
Peters, M. I. and Reimanis, I. E.: Grain boundary grooving studies of yttrium aluminum garnet (YAG) bicrystals, J. Am. Ceram. Soc., 86, 870–872, 2003.
Rabkin, E., Klinger, L., Izyumova, T., Berner, A., and Semenov, V.: Grain boundary grooving with simultaneous grain boundary sliding in Ni-rich NiAl, Acta Mater., 49, 1429–1438, 2001.
Rabkin, E., Gabelev, A., Klinger, L., Semenov, V., and Bozhko, S.: Grain boundary grooving in molybdenum bicrystals, J. Mater. Sci., 41, 5151–5160, 2006.
Rimstidt, J. D. and Barnes, H. L.: The kinetics of silica-water reactions, Geochim. Cosmoch. Ac., 44, 1683–1699, 1980.
Robertson, W. M.: Grain-boundary grooving bysurface diffusion for finite surface slopes, J. Appl. Phys., 42, 463–467, doi:10.1063/1.1659625, 1971.
Saylor, D. M. and Rohrer, G. S.: Measuring the influence of grain-boundary misorientation on thermal groove geometry in ceramic polycrystals, J. Am. Ceram. Soc., 82, 1529–1536, 1999.
Schutjens, P. M. T. M.: Experimental compaction of quartz sand at low effective stress and temperature conditions, J. Geol. Soc. Lond., 148, 527–539, 1991.
Siggia, E. D.: High rayleigh number convection, Annu. Rev. Fluid Mech., 26, 137–168, 1994.

SED
5, 609–654, 2013

Smith, D. L. and Evans, B.: Diffusional crack healing in quartz, J. Geophys. Res., 89, 4125–4135, 1984.
Sotin, C. and Poirier, J. P.: Analysis of high-temperature creep experiments by generalized nonlinear inversion, Mecha. Mater., 3, 311–317, 1984.
Suzuki, S. and Kuroiwa, D.: Grain-boundary energy and grain-boundary groove angles in ice, J. Glaciol., 11, 265–277, 1972.
Tenthorey, E., Cox, S. F., and Todd, H. F.: Evolution of strength recovery and permeability during fluid-rock reaction in experimental fault zones, Earth Planet. Sci. Lett., 206, 161–172, doi:10.1016/S0012-821X(02)01082-8, 2003.
Tester, J. W., Worley, W. G., Robinson, B. A., Grigsby, C. O., and Feerer, J. L.: Correlating quartz dissolution kinetics in pure water from 25-degrees-C to 625-degrees-C, Geochim. Cosmoch. Ac., 58, 2407–2420, 1994.
Thompson, C. V.: Grain growth in thin films, Annu. Rev. Mater. Sci., 20, 245–268, 1990.
Urai, J. L., Williams, P. F., and van Roermund, H. L. M.: Kinematics of crystal growth in syntectonic fibrous veins, J. Struct. Geol., 13, 823–836, doi:10.1016/0191-8141(91)90007-6, 1991.
Watson, E. B. and Wark, D. A.: Diffusion of dissolved SiO_2 in H_2O at 1 GPa, with implications for mass transport in the crust and upper mantle, Contrib. Mineral. Petrol., 130, 66–80, 1997.
Weill, D. F. and Fyfe, W. S.: The solubility of quartz in H_2O in the range 1000–4000 bars and 400–550 °C, Geochim. Cosmochim. Ac., 28, 1243–1255, doi:10.1016/0016-7037(64)90126-7, 1964.
Zhang, W., Sachenko, P., and Schneibel, J. H.: Kinetics of thermal grain boundary grooving for changing dihedral angles, J. Mater. Res., 17, 1495–1501, 2002.
Zhang, W., Sachenko, P., and Gladwell, I.: Thermal grain boundary grooving with anisotropic surface free energies, Acta Mater., 52, 107–116, 2004.

SED
5, 609–654, 2013

Table 1. Parameters of analytical models for grooving controlled by indicated diffusion processes (Mullins 1957, 1960),

diffusion process	exponent	B_i	$\lambda_{d,w}$
diffusion through the solid	$n = 3$	$B_v = \frac{D_v \gamma_s \Omega}{\kappa T}$	$\lambda_d = 1.01, \quad \lambda_w = 5$
diffusion through the liquid	$n = 3$	$B_l = \frac{D_l C_0 \gamma_s \Omega^2}{\kappa T}$	$\lambda_d = 1.01, \quad \lambda_w = 5$
diffusion along the interface of solid and liquid	$n = 4$	$B_s = \frac{D_s \gamma_s \Omega \delta}{\kappa T}$	$\lambda_d = 0.973, \quad \lambda_w = 4.6$

Ω – molecular (atomic) volume ($1.13 \cdot 10^{-28}\,m^3$)
γ_s – surface free energy per unit area ($1\,J\,m^{-2}$)
δ – thickness of the layer in which surface diffusion takes place (2 nm)
κ – Boltzman constant
D_i – diffusion coefficient with $D_i = D_{0,i} \exp\left(-\frac{E_i + pV_i}{RT}\right)$
C_0 – equilibrium concentration of solute in the solvent calculated from m_{sat} – (Eq. 4) (ranges from $1.2 \cdot 10^{25}$ to $4 \cdot 10^{25}$ atoms m^{-3} with run temperature and pressure)
n – growth exponent

SED
5, 609–654, 2013

Table 2. Conditions of the conducted hydrothermal annealing experiments. (*: samples used to calculate the kinetics parameters).

sample	temperature T, (°C)	pressure p, (MPa)	annealing time t, (h)
sequential experiments			
P40, run 1	392	200	5.7
run 2	392	198	3
run 3	392	177	2
P43, run 1	441	198	4
run 2	490	199	21.8
experiments with added SiO_2 powder			
P36	392	209	24
P31	490	201	24
P32	490	200	8
single condition experiments			
P47*	392	194	7.5
P22	392	63	24
P11	392	198	24
P44*	392	202	24
P23	392	399	24
P57*	392	201	48
P51*	392	98	72
P10	392	194	72
P53*	392	292	72
P45*	392	198	96
P20	392	188	120
P37	441	203	2
P25	441	200	8
P27	441	200	24
P17	441	202	72

SED
5, 609–654, 2013

Table 2. Continued.

sample	temperature T, (°C)	pressure p, (MPa)	annealing time t, (h)
P8	490	198	2
P12	490	208	8
P15	490	192	72
P48*	568	200	0.09
P30	568	64	2
P42*	568	204	4
P21	568	202	8
P50*	568	100	24
P46*	568	205	24
P54	568	260	47.7
P38	568	202	48

SED
5, 609–654, 2013

Table 3. Results from fit of growth law (3) to observations of $d/\cot\delta$.

diffusion path	pre-factor D_0 ($m^2\,s^{-1}$)	activation energy E ($kJ\,mol^{-1}$)	activation volume V ($cm^3\,mol^{-1}$)
through crystal	$3\cdot10^{-12\pm2}$	113 ± 24	-104 ± 37
through fluid volume	$3\cdot10^{-9\pm2}$	115 ± 23	-98 ± 37
interface diffusion	$4\cdot10^{-8\pm2}$	133 ± 25	-105 ± 37

SED
5, 609–654, 2013

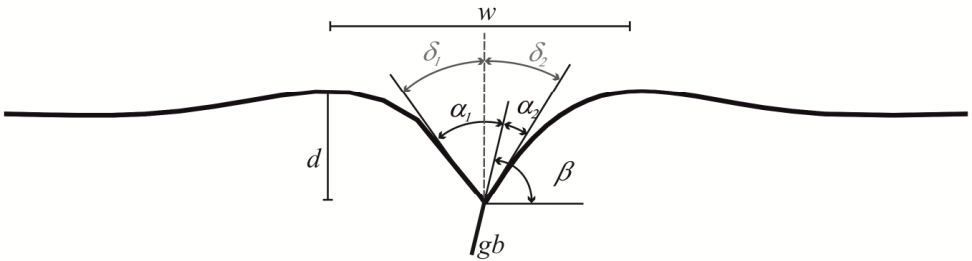

Fig. 1. Sketch illustrating the parameters characterizing groove geometry. The distance between humps is termed groove width w, the distance between groove root and a hump is termed groove depth d. The grain boundary (gb) encloses an angle β with the surface of the polycrystall and the two sides of the groove are inclined by angles $\delta_{1,2}$ to the normal.

SED
5, 609–654, 2013

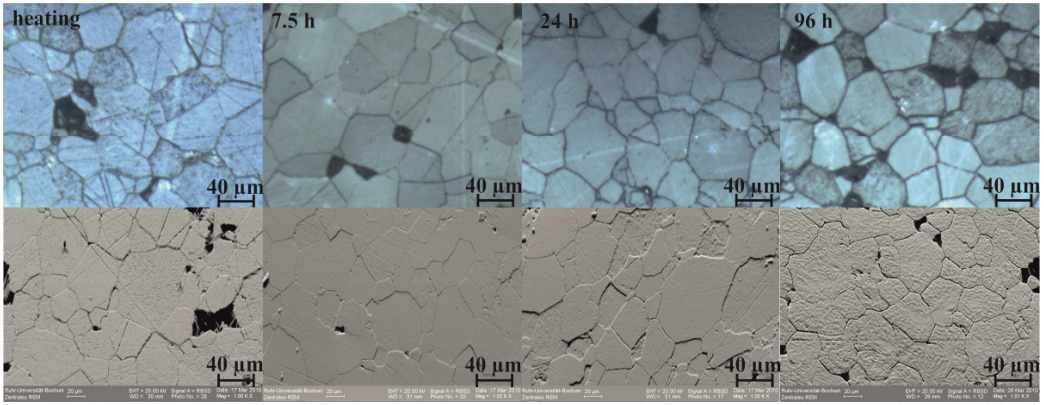

Fig. 2. Sample surfaces as observed with light microscope (top row) and SEM (bottom row) for samples annealed at 392 °C for 7.5, 24, and 96 h. The images labeled heating show a sample that experienced heating up to 568 °C at 200 MPa and immediate cooling.

SED
5, 609–654, 2013

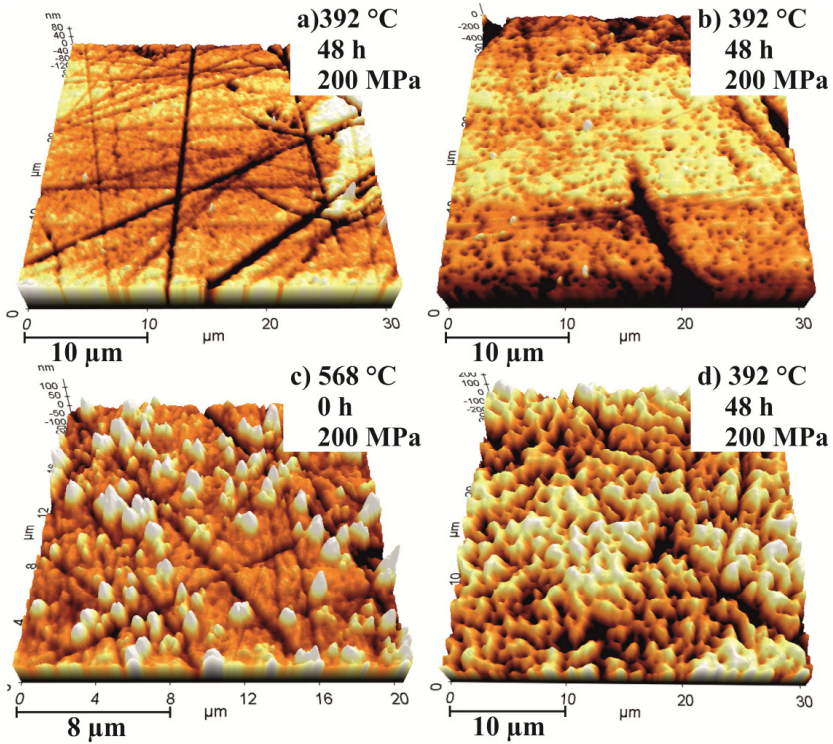

Fig. 3. General surface characteristics of hydrothermally annealed samples as observed with AFM. The images represent dissolution (first row) and growth structures (second row) for different crystallographic surfaces. **(a)** $\{10\bar{1}0\}$ surface with scratches of different depths up to 70 nm; **(b)** $\{10\bar{1}1\}$ surface with holes (10 to 50 nm); Growth structure: **(c)** selected pocks found at low lying grains, **(d)** {0001} surface with strong roughness found at high lying grains (Relief differences with range from 100 to 200 nm). The images **(a)**, **(b)** and **(d)** were measured at the same sample (P57, see Table 2).

SED
5, 609–654, 2013

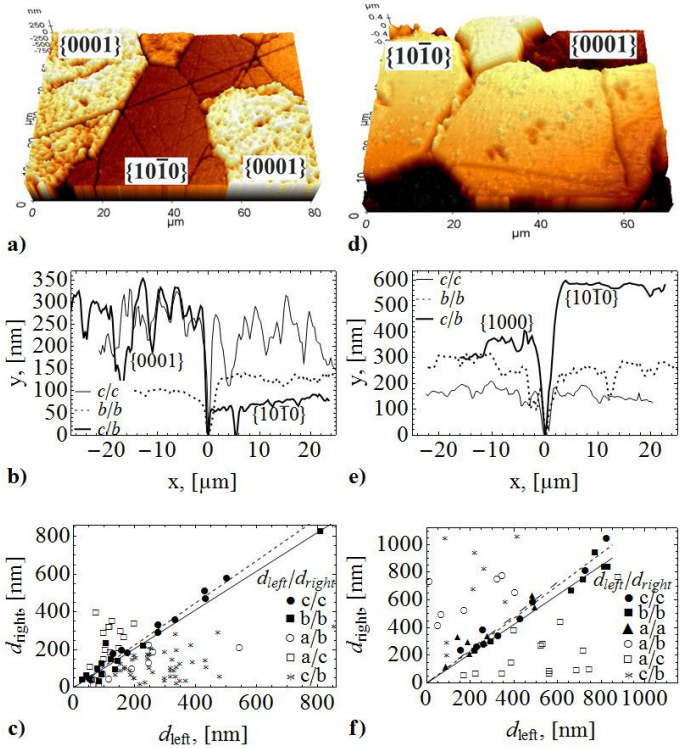

Fig. 4. Orientation dependence of height difference between grains after annealing at 392 °C for 48 h (**a** to **c**) and at 568 °C for 4 h (**d** to **f**). **(a)** and **(d)** AFM image with {0001} and {10$\bar{1}$0} surfaces, **(b)** and **(e)** Profile normal to grain boundary, x/x describes the surface orientation of neighboring grains where a denotes {11$\bar{2}$0}, **(b)** {0001}, and **(c)** {10$\bar{1}$0} surfaces, **(c)** Relation between groove depth of left and right groove sides and orientation. For the same grain orientation the data locate on the bisecting.

SED
5, 609–654, 2013

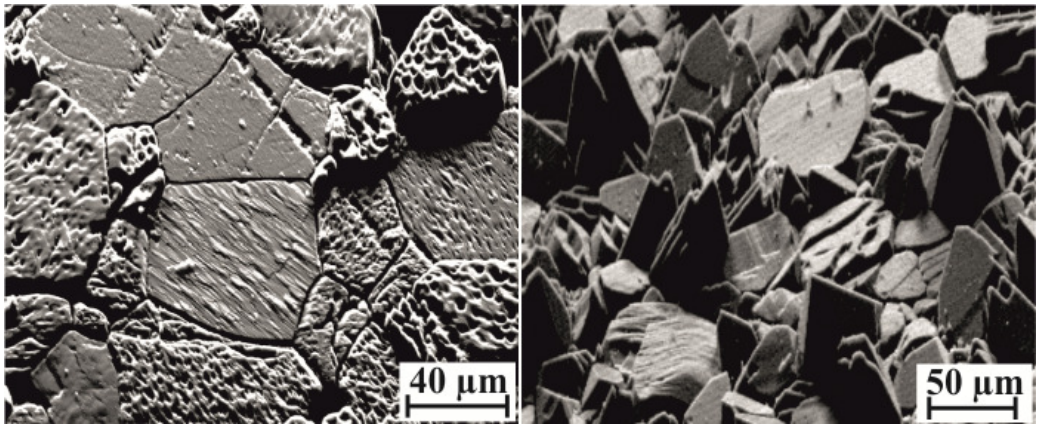

Fig. 5. SEM images indicate differences in development of specific crystallographic surfaces for 441 °C 72 h, 195 MPa (right) and 568 °C, 47 h 260 MPa (left).

SED
5, 609–654, 2013

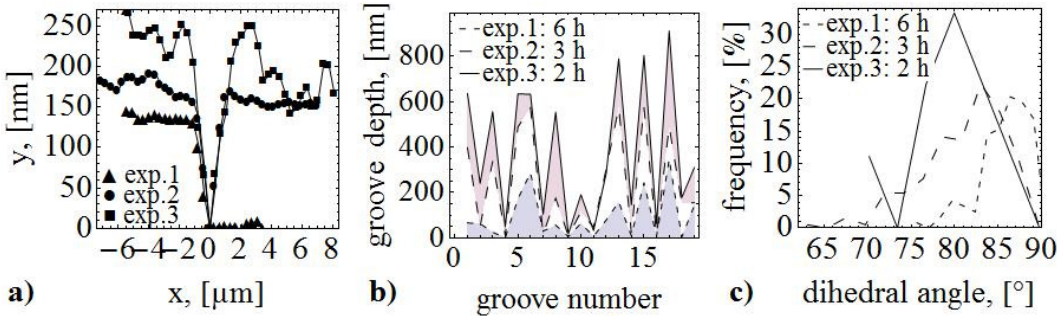

Fig. 6. Evolution of **(a)** groove profiles, **(b)** groove depth and **(c)** dihedral angle in sequential 765 experiments at 392 °C (P40 1–3, see Table 2).

SED
5, 609–654, 2013

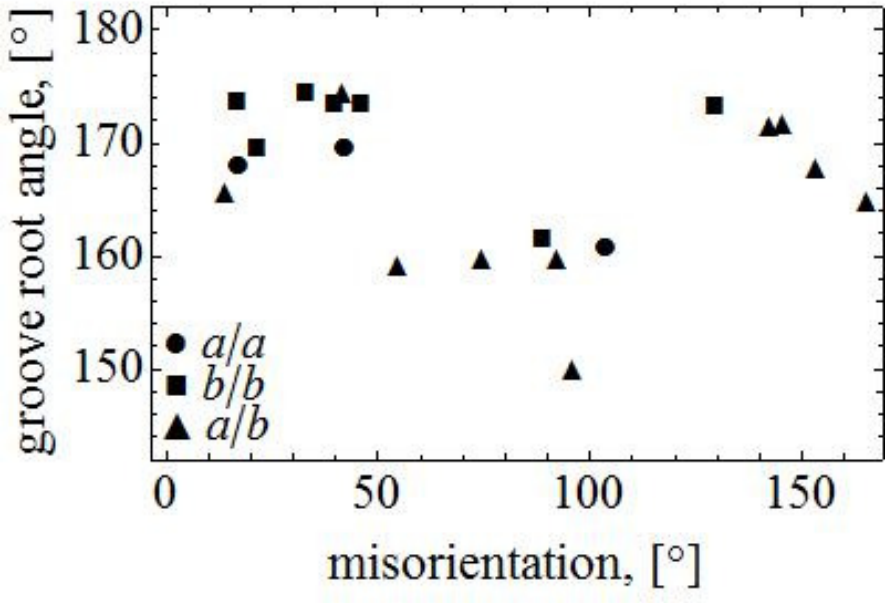

Fig. 7. Relation between observed groove-root angle and misorientation between neighboring grains with *a* or *b* axes normal to the sample surface quantified by the angle between the *c*-axes of the neighboring grains.

SED
5, 609–654, 2013

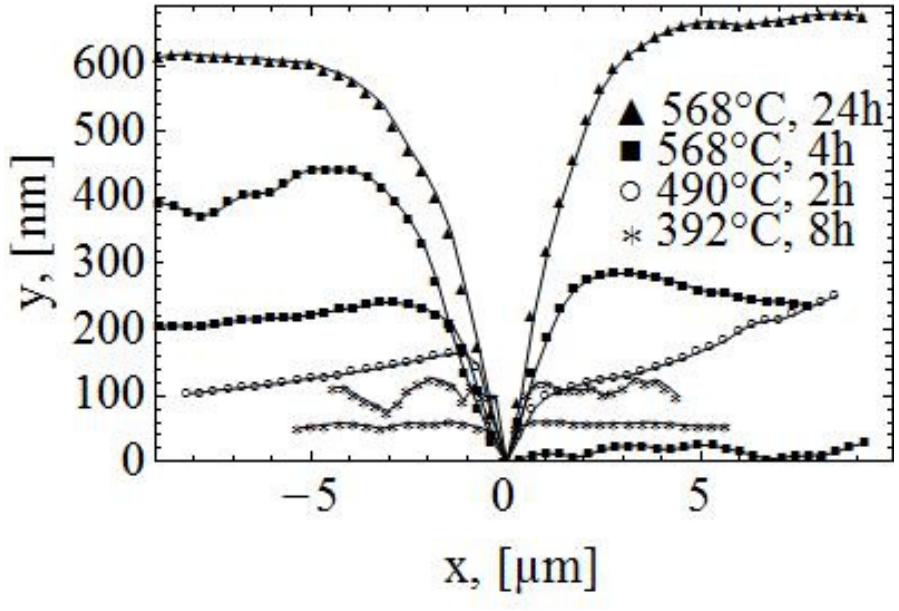

Fig. 8. Examples of observed groove geometries after indicated annealing conditions.

SED
5, 609–654, 2013

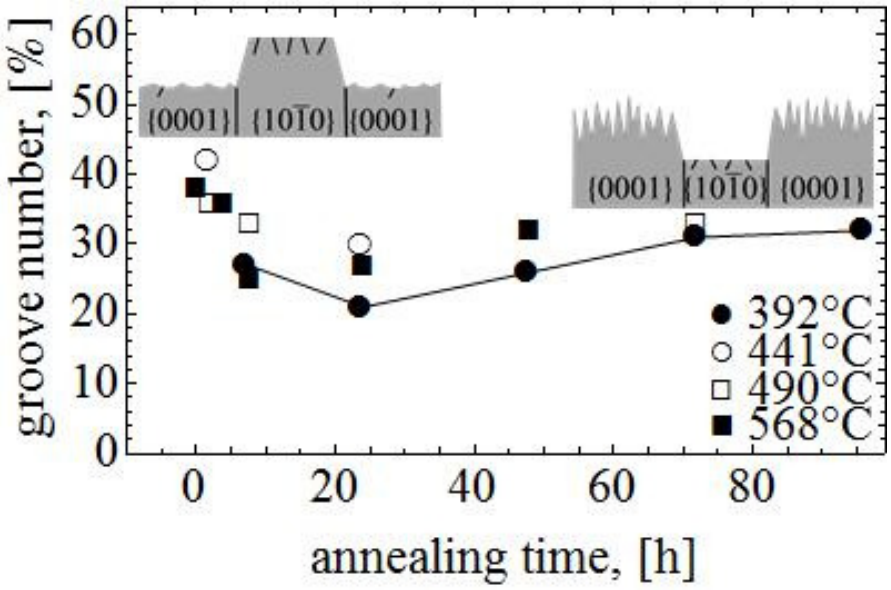

Fig. 9. Evolution of the fraction of grooves identified to be due to dissolution. The images show schematically differences in surface geometry for long and short experiments (see also Fig. 4) for which a switch from preferential dissolution of {0001} surfaces to preferential growth on {0001} surfaces is observed.

SED
5, 609–654, 2013

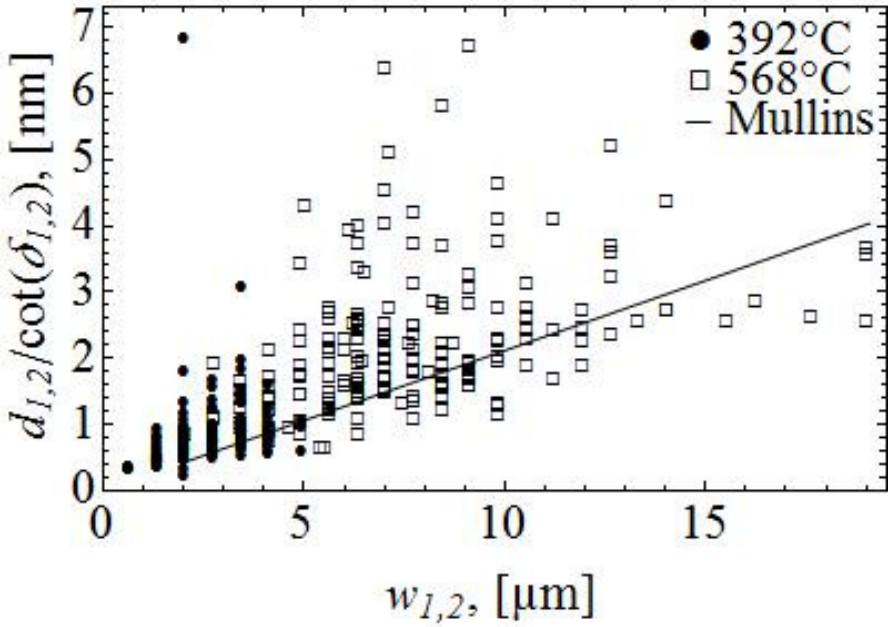

Fig. 10. Cross-correlation of weighted groove depth and groove width for annealing at indicated temperatures and duration of 24 h. The line represents the expected correlation according to the Mullins theory (see Eqs. 5 and 6).

SED
5, 609–654, 2013

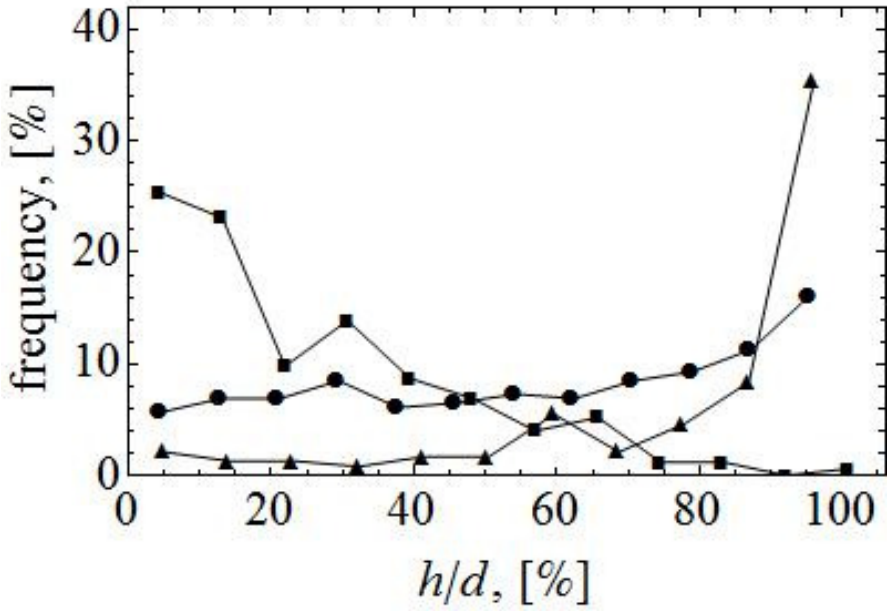

Fig. 11. Observed frequency of step height normalized by groove depth after annealing at 392 ˚C for indicated durations.

SED
5, 609–654, 2013

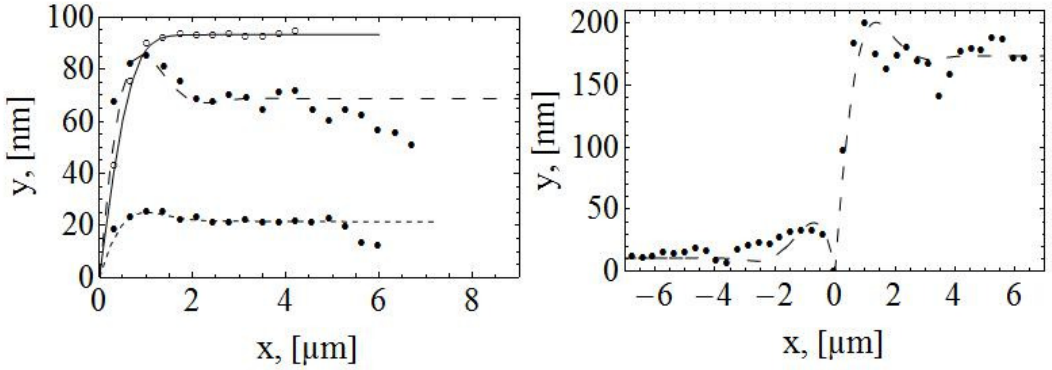

Fig. 12. Fit of theoretical groove shape (Mullins theory) to individual groove profiles (points) observed for an annealing experiment at **(a)** 392 °C and 7.5 h and **(b)** 392 °C and 48 h ($D_{S,S} = 1.6 \cdot 10^{-14}\,m^2\,s^{-1}$, $\delta_1 = 83.7°$, $\delta_1 = 83.7°$, $\alpha = 0.16$). The line styles of the fitted model curves are chosen such that solid, long dashed or short dashed lines correspond to grooving kinetically controlled by dissolution ($m[SiO_2] = 4 \cdot 10^{-10}\,mol\,kg^{-1}, m^2\,s^{-1}$, $\delta = 83°$), by surface diffusion ($D_{S,S} = 3.6 \cdot 10^{-14}\,m^2\,s^{-1}$, $\delta = 77°$) or by diffusion through liquid ($D_{S,l} = 9.5 \cdot 10^{-14}\,m^2\,s^{-1}$, $\delta = 86.5°$), respectively.

SED
5, 609–654, 2013

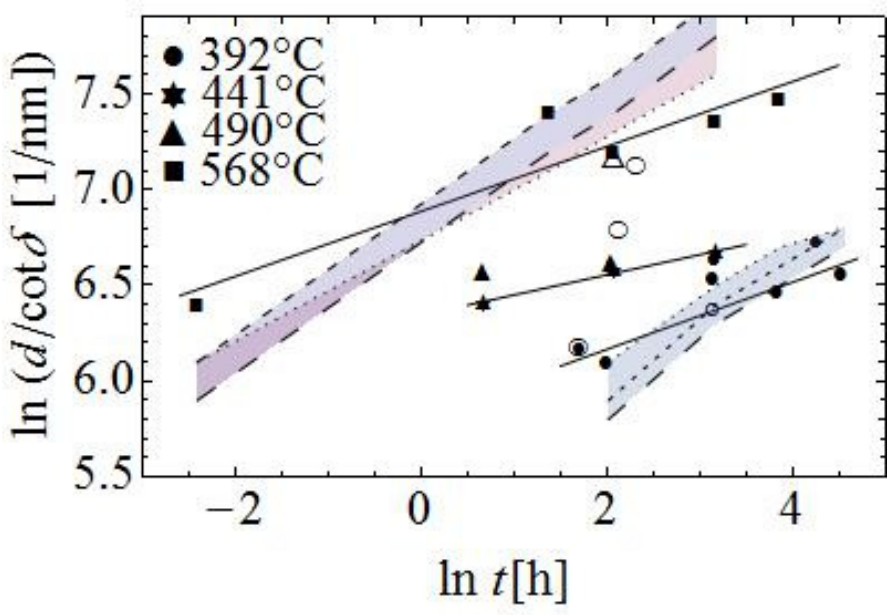

Fig. 13. Correlation of the ratio of groove depth and cotangent of groove-root angle and annealing time for experiments run at indicated temperatures. Only those grooves were used to determine average groove parameters at given conditions that exhibit a width-depth ratio that does not deviate from the value of the Mullins theory by more than 0.1 (see Eqs. 3 and 4). The dashed lines indicate the results of the inversion for kinetics parameters of the three considered scenarios, surface diffusion (dotted line), diffusion through liquid (short dashed) and volume diffusion (long dashed) (Eq. 4, Table 3). The open symbol represents the experiments with SiO_2 powder. The large circle symbols indicate the sequential experiment.

SED
5, 609–654, 2013

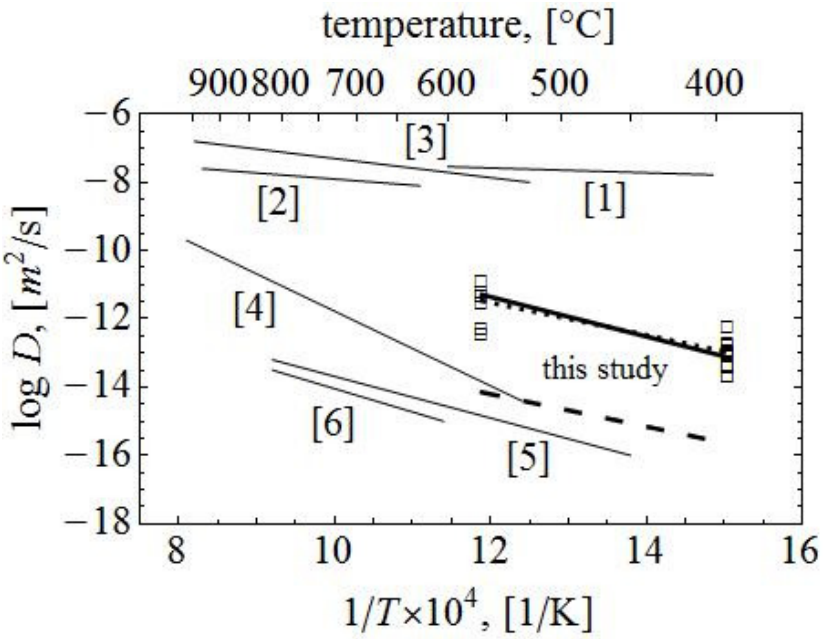

Fig. 14. Diffusion coefficients constrained by the analyses performed in this study in comparison to previously reported values. Open squares represent the results from fitting individual grooves by the analytical groove shapes suggested by the Mullins theory (see also Fig. 12). The lines labeled "this study" represent the results from fitting sets of groove characteristics (see also Fig. 13, Eqs. 3 and 4 with kinetics data from Table 3). Thin solid lines refer to literature values: [1] Stokes–Einstein relation for 1 GPa (Watson and Wark, 1997); [2] SiO_2 diffusivity at 1 GPa (Watson and Wark, 1997); [3] diffusion of $Si(OH)_4$ in bulk water at 900 °C, 500 MPa (Doltsinis et al., 2007a); [4] grain boundary diffusion of SiO_2 constrained by growth rates of wollastonite rims observed in contact metamorphic rocks (Joesten and Fisher, 1988); [5] hydrothermal grain boundary diffusion of O (Farver and Yund, 1991); [6] hydrothermal grain boundary diffusion of Si for 600–800 °C, 150 MPa, (Farver and Yund, 2000).

SED
5, 609–654, 2013

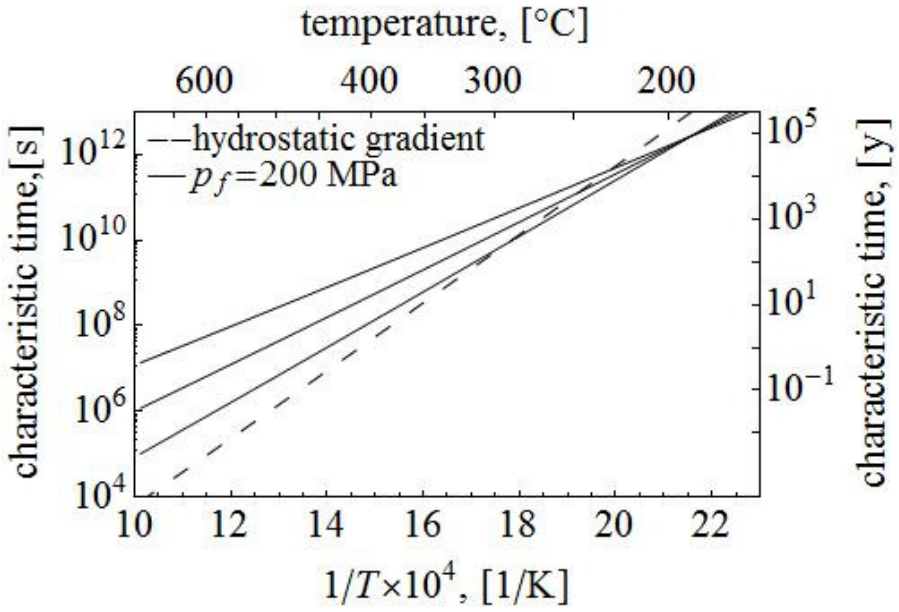

Fig. 15. Prediction of characteristic time for crack healing according to Eq. (8) using the constraints on kinetics parameters for surface diffusion as rate-controlling mechanism (Table 3). A crack width of 1 µm is assumed in the calculations. Calculations were performed for a constant fluid pressure (solid lines) and a fluid pressure-temperature relation according to a geotherm of 30 K km^{-1} and a hydrostatic pressure gradient. The thin solid lines explicitly indicate the uncertainty in the prediction for a constant fluid pressure resulting from the quoted uncertainty in kinetics parameters. A similar range results for the model with fluid pressure following a hydrostatic gradient.

SED
5, 609–654, 2013